Journal of Materials Chemistry A

ROYAL SOCIETY OF CHEMISTRY

COMMUNICATION

View Article Online
View Journal | View Issue

Cite this: *J. Mater. Chem. A*, 2021, 9, 8966

Received 17th February 2021
Accepted 12th March 2021

DOI: 10.1039/d1ta01422f

rsc.li/materials-a

Highly reversible aluminium–sulfur batteries obtained through effective sulfur confinement with hierarchical porous carbon†

Dian Zhang,‡[a] Xu Zhang, ‡[a] Boya Wang,[a] Shiman He,[a] Shiqi Liu, [a] Mingxue Tang[b] and Haijun Yu *[a]

Aluminium–sulfur (Al–S) batteries possess high research merits and application prospects owing to their high theoretical energy density, high safety and low cost. However, the deficiency of outstanding cathodes severely limits their electrochemical performance. Herein, a N-doped hierarchical porous carbon material with a surface area of 2513 m^2 g^{-1} has been developed by a soft-template method. The hierarchical pores can provide effective electrolyte transport channels and stably accommodate S nanoparticles, while the N-doped carbon can facilitate charge transfer and anchor aluminium sulfides to improve the electrochemical stability of the cathode. Coupling the S composite cathode with a low-cost $AlCl_3$/acetamide electrolyte, the Al–S battery can deliver a capacity above 1027 mA h g^{-1} at 0.2 A g^{-1} for 50 cycles and an excellent cyclability above 483/405 mA h g^{-1} at 1 A g^{-1} for 500/700 cycles. *In situ* Raman spectroscopy and *ex situ* solid-state nuclear magnetic resonance have been used to monitor the reversible reactions of S and identify the configuration of sulfides, showing that α-type Al_2S_3 with a tetra-coordinated configuration is the dominant final discharge product. This work sheds light on the design of S composite cathodes and understanding of reaction mechanisms for the fabrication of high-reversibility, high-capacity and low-cost Al–S batteries.

1. Introduction

The rapidly developed beyond-lithium-based batteries provide prospective alternatives to the resource-limited lithium-based batteries to boost large-scale and cost-efficient energy storage applications.[1,2] Among them, aluminium-ion batteries (AIBs) have recently attracted broad attention owing to the high theoretical capacity (2980 mA h g^{-1} or 8046 mA h cm^{-3}), abundant resources and high safety of the Al anode.[3–6] A lot of materials have been attempted as cathodes to couple with the Al anode, such as carbon-based materials,[3,7–13] metal oxides,[14–17] metal sulfides,[18–21] sulfur (S),[22–30] and selenium (Se).[6,31,32] Considering the ultrahigh theoretical capacity (1675 mA h g^{-1}), low cost, and eco-friendliness of S, rechargeable Al–S batteries are ranked as one of the most promising AIBs for practical applications, which have not been extensively studied so far.

Despite the considerable advantages, Al–S batteries are greatly impeded by some obstacles toward practical applications. The immature materials in Al–S batteries, especially the conversion-type S cathode, introduce diverse drawbacks including a low conductivity, sluggish kinetics, large volume change, possible "shuttle effect" of polysulfide intermediates, large voltage hysteresis, *etc.*[22,26,27] These drawbacks will worsen the electrochemical reversibility of the Al–S system, inducing a great demand for delicately designed S composite cathodes to improve the cyclability. Considering the cathode design, a noticeable fact is that the same S composite cathode may deliver much worse electrochemical reversibility in Al–S batteries than that in Li–S batteries,[24,26,33,34] which may be attributed to the distinct electrolytes and derived reaction mechanisms. For example, the room-temperature viscosity and conductivity of the $AlCl_3$/acetamide (AcA) electrolyte for Al–S batteries are several tens of times larger and around ten times smaller than those of the commonly used 1 M lithium bis(trifluoromethanesulfonyl)imide in 1,2-dimethoxyethane/1,3-dioxolane (1 : 1 by volume) electrolyte for Li–S batteries, respectively.[35–38] Thus the electrolyte transport and the charge transfer in Al–S batteries are much more difficult. Therefore, there is an ultrahigh demand for the design of host materials to fabricate high-performance S composite cathodes, which should have specific compatibility to Al–S batteries.

The electrolyte is another critical factor that determines the electrochemical performance of Al–S batteries. For example, a Li^+-mediated $AlCl_3$/1-ethyl-3-methylimidazolium chloride

[a]College of Materials Science and Engineering, Faculty of Materials and Manufacturing, Beijing University of Technology, Beijing, 100124, China. E-mail: hj-yu@bjut.edu.cn

[b]Center for High Pressure Science & Technology Advanced Research, Beijing, 100094, China

† Electronic supplementary information (ESI) available. See DOI: 10.1039/d1ta01422f

‡ The two authors contributed equally to this work.

(EMICl) ionic liquid (IL) electrolyte has been employed to optimize the electrochemical performance and the derived Al–S battery could maintain a capacity of 600 mA h g^{-1} after 50 cycles.[23] Unfortunately, most of the reported electrolytes for Al–S batteries are $AlCl_3$-based ILs, which are inappropriate for large-scale applications owing to their high cost and strong corrosivity.[5] It is thus necessary to develop high-performance Al–S batteries based on low-cost electrolytes.

The electrochemical behaviors of Al–S batteries are important to understand their degradation mechanism and enhance their performance by purposeful material design. However, there are many unclear issues about the reaction mechanism of the Al–S electrochemistry. For example, the detailed formation process and configurations of the discharge products, which are important to better harness the Al–S electrochemistry, have not been well elucidated. The effects and mechanisms of diverse S hosts on favoring the electrolyte transport, facilitating the interfacial charge transfer, and stabilizing the S species are also not well understood. To this end, advanced characterization techniques are required to be introduced into the Al–S system.

Recently, we have demonstrated a low-cost deep eutectic solvent $AlCl_3$/acetamide (molar ratio: 1.3/1, $AlCl_3$/AcA (1.3/1) for short) electrolyte for Al–S batteries.[24] However, there is still a lot of scope to improve the electrochemical performance of the $AlCl_3$/AcA-based Al–S battery, especially the capacity and reversibility. Herein, we developed a N-doped hierarchical porous carbon material to effectively confine S species for high-capacity, high-reversibility and low-cost Al–S batteries. The carbon material provides hierarchical micro-, meso-, and macro-pores with a high specific surface area to provide fast electrolyte transport channels and to promote the stable confinement of S nanoparticles, and the N-doped carbon facilitates the charge transfer during electrochemical reactions and chemical anchoring of S-containing species. Coupled with a low-cost $AlCl_3$/AcA (1.3/1) electrolyte, the composite cathode could deliver largely improved performance, especially the long-cycle performance. The reaction mechanism of the Al–S electrochemistry was well elucidated by combining XPS (X-ray photoelectron spectra), *in situ* Raman spectroscopy and solid-state nuclear magnetic resonance (ssNMR). The study paves the way for compatible S cathode design for highly reversible Al–S batteries.

2. Results and discussion

To fabricate a high-performance S@C composite cathode compatible with Al–S batteries, we developed a new approach to prepare a N-doped hierarchical porous carbon (HPCK) material as the S loading material. Fig. 1 shows the preparation procedures of HPCK and the subsequent fabrication of the S@HPCK composite cathode, and the synthesis details are provided in the Experimental section in the ESI.†

First, a paraformaldehyde condensation with 4,4′-methylenedianiline (MDA) was performed in *N*-methyl pyrrolidone (NMP) together with well-dissolved zinc nitrate hydrate ($Zn(NO_3)_2 \cdot 6H_2O$) as a pore former to produce a N-rich polymer.[39] The polymer was then carbonized in argon at 10 kPa and

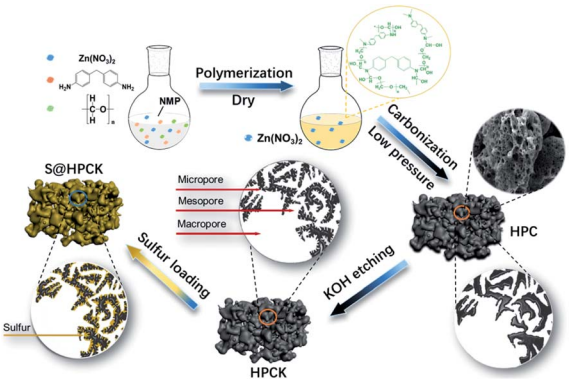

Fig. 1 Schematic illustration of the preparation of HPCK and S@HPCK.

900 °C with a ramp rate of 2 °C min^{-1} to form an unmodified N-doped hierarchical porous carbon (HPC) material, during which the $Zn(NO_3)_2 \cdot 6H_2O$ decomposed and evaporated to produce macro-, meso-, and micro-pores in the derived carbon material. To further tune the pore distribution, improve the specific surface area and create more chemisorption sites, HPC was then etched with KOH to reshape mesopores and produce more micropores. Finally, the KOH-etched HPC (HPCK) was employed to accommodate S at 155 °C driven by the pore confinement and adsorption effects.

The paraformaldehyde condensation yielded a viscous solution containing the N-rich polymer precursor and well-dissolved $Zn(NO_3)_2 \cdot 6H_2O$ (Fig. S1†), which was converted into a foam-like carbon material (HPC) after carbonization (Fig. S2†). Fig. S3† shows the SEM images of the derived foam-like HPC. It contains many macropores separated by ~100–500 nm thick carbon walls, where distinguishable mesopores are distributed. Furthermore, the as-prepared HPC was further etched with KOH to tailor the pore structure, increase the surface area and create more active sites to host sulfur with higher loading capability, more stable confinement and higher reaction efficiency. The SEM image of HPCK in Fig. 2a indicates the good maintenance of the HPC foam-like framework, while the high-resolution SEM image of the HPCK foam wall in Fig. 2b displays highly mesoporous structures. The EDS mapping shows a uniform distribution of doped N as well as residual O within the C matrix (Fig. S4†). HPCK was further subjected to TEM investigation to identify its porous structure. As shown in Fig. 2c, many pores appearing as white spots can be observed in the HPCK slice, demonstrating the existence of mesopores and micropores. These pores can also be identified in the high-resolution TEM image in Fig. 2d by their light contrast. The surrounding carbon structures are identified to be dominantly amorphous, in line with the Raman spectrum of HPCK with a strong defect-correlated D band (Fig. S5†).

The pore configurations of HPC and HPCK have been further analyzed by the N_2 isothermal adsorption technique. It was found that HPC has a typical hysteresis loop in the N_2 adsorption–desorption isotherm profile (Fig. S6†), which has been reshaped by KOH etching with a more noticeable hysteresis loop and increased N_2 adsorption (Fig. 2e and S6†). Consequently, compared with HPC, HPCK possesses a significantly

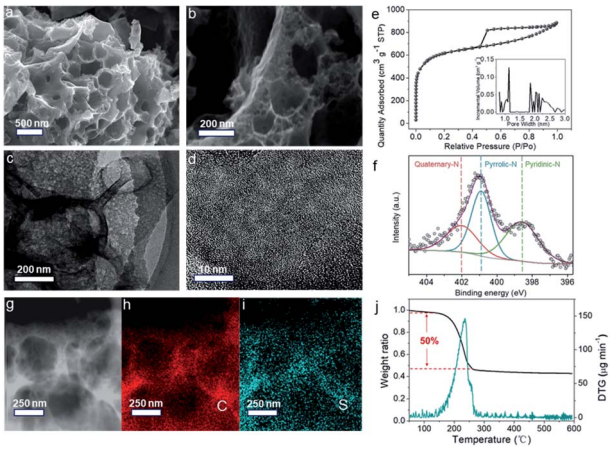

Fig. 2 Structural investigations on the HPCK and S@HPCK composite. (a, b) Scanning electron microscope (SEM) and (c, d) transmission electron microscope (TEM) images of HPCK. (e) The nitrogen adsorption–desorption isotherm profile and pore size distribution (inset). (f) High-resolution XPS N 1s spectra of HPCK. (g) TEM image of S@HPCK and (h ang i) corresponding Energy Dispersive Spectroscopy(EDS) maps of C and S. (j) Thermal Gravimetric Analysis (TGA) and Derivative Thermogravimetric Analysis (DTG) profiles of S@HPCK in a N_2 atmosphere.

improved BET surface area (2513 $m^2\ g^{-1}$ *vs.* 1234 $m^2\ g^{-1}$) and pore volume (1.24 $cm^3\ g^{-1}$ *vs.* 0.785 $cm^3\ g^{-1}$). Moreover, the pore size of HPCK is largely distributed in the range of <3 nm, indicating a large number of micropores (inset of Fig. 2e). As can be seen from the pore size distribution in Fig. S7,† HPC and HPCK have basically the same porous distribution above 5 nm, while HPCK has more micro- and meso-pores in the range of 0.6–3 nm. This suggests that the aforementioned basic foam-like framework and macropores of HPC were preserved, while more micro- and meso-pores were created by the KOH etching. The hierarchical pore configuration of HPCK with a high surface area and a large fraction of micropores can well confine S nanoparticles and promote electrolyte infiltration for high reaction efficiency, while the macropores provide fast transport channels for the relatively viscous $AlCl_3$/AcA electrolyte.

The N-doping nature of HPCK revealed by the EDS analysis has been further demonstrated by XPS (Fig. S8†), showing that HPCK has a high N content of 5.2 at%. The high-resolution N 1s spectrum in Fig. 2f can be deconvoluted into three types of N moieties including pyridinic N at 398.6 eV, pyrrolic N at 400.9 eV and quaternary N at 402 eV,[40] with a corresponding area ratio of ~5 : 5 : 3. The high contents of pyridinic N and pyrrolic N are beneficial for anchoring polysulfides in carbon hosts,[41,42] owing to the chemisorption effects between N and S-containing species (see below, Fig. 5c and d). An improved cycle stability of the S@HPCK composite cathode in Al–S batteries is thus anticipated.

HPCK was then used to accommodate S by heating a mixture of 50 wt% S and 50 wt% HPCK in a sealed container at 155 °C for 12 h. The XPS survey spectra of HPCK and S@HPCK in Fig. S8† clearly show the appearance of S signals for the latter. Meanwhile, the Raman spectrum of S@HPCK shows characteristic S peaks at ~150, 220 and 480 cm^{-1} aside from the D and G peaks belonging to HPCK, which also confirms the successful S loading (Fig. S9†). The TEM image of the as-prepared S@HPCK composite cathode in Fig. 2g indicates the absence of large S particles, implying the dominant encapsulation of S into meso- and micro-pores. Fig. S10† shows that some ~1–4 nm S crystallites are imbedded inside the meso- and micro-pores of HPCK. Furthermore, a comparison between the X-ray diffraction (XRD) patterns of S@HPC and S@HPCK indicates a different confinement feature of S (Fig. S11†). S@HPC exhibits apparent S crystal patterns, whereas S@HPCK shows no distinguishable S pattern, indicating that most S in S@HPCK lost the original long-range order owing to its minimized sizes during the melting and encapsulation process. Consequently, the distribution of S inside HPCK is uniform, as revealed by the corresponding EDS maps in Fig. 2h and i. The thermal gravimetric analysis (TGA) of S@HPCK under argon in Fig. 2j indicates ~50 wt% S in S@HPCK, suggesting the high efficiency of S loading in HPCK. Note that the 50 wt% S content is among the highest values for the state-of-the-art S composite cathodes for Al–S batteries. A S@HPCK composite with a loading amount of 70 wt% was also achievable (Fig. S12†).

The electrochemical performance of the S@HPCK cathode has been evaluated in an Al–S battery, coupled with Al foil as the anode and $AlCl_3$/AcA (1.3/1) as the electrolyte. Fig. S13† shows the Raman spectrum of the $AlCl_3$/AcA (1.3/1) electrolyte, with two strong peaks assigned to $[AlCl_4]^-$ at 347 cm^{-1} and $[Al_2Cl_7]^-$ at 312 cm^{-1}.[43,44] In this electrolyte, the S@HPCK cathode shows a typical S redox chemistry revealed by Cyclic Voltammetry (CV) curves (Fig. S14a†). Moreover, the CV curves of the S@HPCK cathode at different scan rates and the corresponding plot of peak current *vs.* the scan rate indicate that the conversion of S in the S@HPCK electrode is dominated by a diffusion-controlled faradaic process, *i.e.*, electrochemical rather than a pseudocapacitive process. The Al–S@HPCK battery with a 50 wt% S content in S@HPCK exhibits discharge and charge capacities of 1330 mA h g^{-1} and 1195 mA h g^{-1} at a current density of 0.2 A g^{-1} in the 1st cycle (Fig. 3a), respectively. Upon electrochemical cycling, the discharge capacity gradually increases to a maximum value of 1583 mA h g^{-1} in the 12th cycle, while the charge capacity increases to a maximum value of 1797 mA h g^{-1} in the 14th cycle.[24] The rising capacity in the initial cycles is likely due to the electrochemical infiltration of the electrolyte for the activation of the Al–S battery. The S@HPCK cathode can deliver high capacities with relatively small attenuation in the subsequent cycles. After 50 cycles, a high discharge capacity of 1027 mA h g^{-1} and a charge capacity of 1131 mA h g^{-1} could still be maintained, with only a minor fraction of capacity contributed by HPCK (Fig. S15†). Compared with previous reports, our S@HPCK composite delivers the most superior discharge capacities within 50 cycles.[22,24]

Fig. 3b displays the galvanostatic discharge/charge voltage profiles in different cycles at 0.2 A g^{-1}. After an activation process, the discharge voltage plateau increases from ~0.6 V in the 2nd cycle to ~0.7 V in the 10th cycle. From the 10th to the 50th cycle, the discharge voltage plateau decreases from ~0.7 V to ~0.55 V, indicating an enlargement of overpotential in further cycles. The charge voltage plateau is about 1.45 V in the 2nd cycle, and then slightly drops to 1.4 V after activation, and

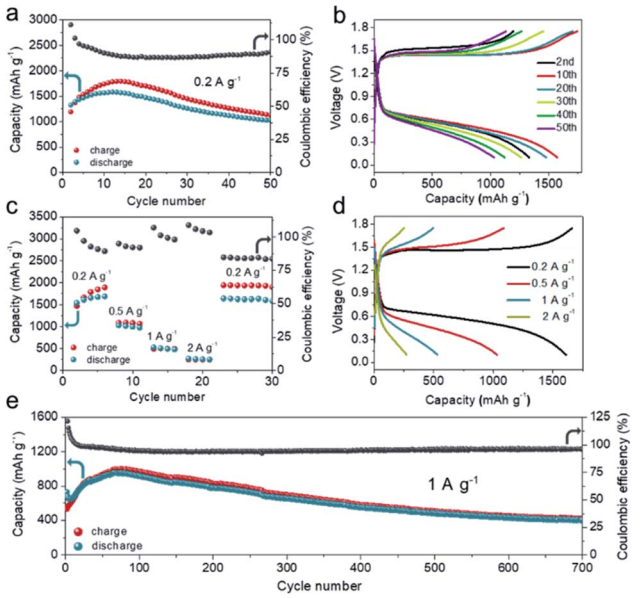

Fig. 3 Electrochemical performance of the Al–S@HPCK battery at 25 °C. (a) Cycling performance under a current density of 0.2 A g^{-1}, and (b) corresponding galvanostatic charge/discharge curves. (c) Rate performance under current densities of 0.2, 0.5, 1 and 2 A g^{-1}, and (d) corresponding galvanostatic charge/discharge curves. (e) Long-term cycle performance under a current density of 1 A g^{-1}.

then remained nearly constant in the following 40 cycles, indicating that the oxidation potential of S is stable. The voltage hysteresis is a general drawback for the current Al–S batteries. Compared with our previous $AlCl_3$/AcA (1.3/1)-based Al–S battery using a S@CMK-3 cathode material,[24] S@HPCK can reduce the voltage hysteresis to some extent, as shown in Fig. S16.†

The rate performance of the Al–S@HPCK battery is displayed in Fig. 3c and d. After the initial activation for 5 cycles at 0.2 A g^{-1}, the cathode delivers discharge capacities of 1090 mA h g^{-1}, 530 mA h g^{-1}, and 272 mA h g^{-1} at 0.5 A g^{-1}, 1 A g^{-1} and 2 A g^{-1}, respectively. When the current density returns to 0.2 A g^{-1}, the discharge capacity recovers to 1639 mA h g^{-1}, close to the theoretical capacity of S (1675 mA h g^{-1}), suggesting the excellent recovery of S redox in the system.

Owing to the compatibility of HPCK with the Al–S electrochemistry, the long-term cycle stability of the battery was improved.[24] As shown in Fig. 3e, the Al–S@HPCK battery can deliver discharge capacities of 483/405 mA h g^{-1} and coulombic efficiencies of 95.3/96.2% in the 500th/700th cycles at 1 A g^{-1}. Although it is not close to 100% owing to the loss of active materials during cycling and possible side reactions,[27] the coulombic efficiency of our Al–S battery is much enhanced compared with that of previously reported Al–S batteries (Table S1, ESI†).[22–27,45,46] Moreover, the Al–S@HPCK battery can stably run over 5000 cycles at 2 A g^{-1}, delivering discharge capacities of 274/130 mA h g^{-1} and coulombic efficiencies of 97/99% in the 1000th/5000th cycles (Fig. S17†).

To evaluate the scale-up feasibility of the Al–S@HPCK chemistry, soft-pack batteries have been assembled and were found to work stably for a long time. Fig. S18† shows that a battery pack can light up a set of LED lights, suggesting the good scale-up feasibility of the S@HPCK cathode for high-performance Al–S batteries.

For practical Al–S batteries, the S loading content is one of the major concerns and unfortunately has not surpassed 50 wt% till now.[24,45] We therefore investigated the electrochemical performance of our S@HPCK composite containing 70 wt% S (Fig. S12†). As shown in Fig. S19,† the corresponding Al–S@HPCK battery delivers an initial discharge capacity of 1341 mA h g^{-1}, which gradually decays in the following cycles after a short activation process. The reduced capacity maintenance of S@HPCK with 70 wt% S may be ascribed to the S particles loaded in the macropores, which have less electrochemical efficiency during cycling because of their poor confinement. Still, a promising discharge capacity of 524 mA h g^{-1} can be maintained after 50 cycles. The discharge/charge profiles of S@HPCK containing 50 and 70 wt% S are compared in Fig. S20,† showing slightly greater polarization for the latter owing to the increased S content. The cycle performances and galvanostatic profiles of $AlCl_3$/AcA and $AlCl_3$/EMICl electrolytes in Al–S@HPCK batteries are shown in Fig. S21,† showing that the $AlCl_3$/AcA electrolyte exhibits better cyclability and less polarization than $AlCl_3$/EMICl. The performances of recently reported Al–S batteries are compared as shown in Table S1,† suggesting the significantly enhanced overall performance of our Al–S battery based on the S@HPCK composite cathode materials coupled with a low-cost $AlCl_3$/AcA electrolyte.

In order to explore the reaction mechanism of the Al–S@HPCK battery, the chemical states of the S cathode in different charged/discharged states were investigated by XPS. As shown in Fig. 4a, the XPS S 2p spectrum of the pristine S@HPCK cathode reveals a typical S_8 structure, with its S 2p1/2 and S 2p3/2 peaks located at 165.2 eV and 164.0 eV, respectively. In the

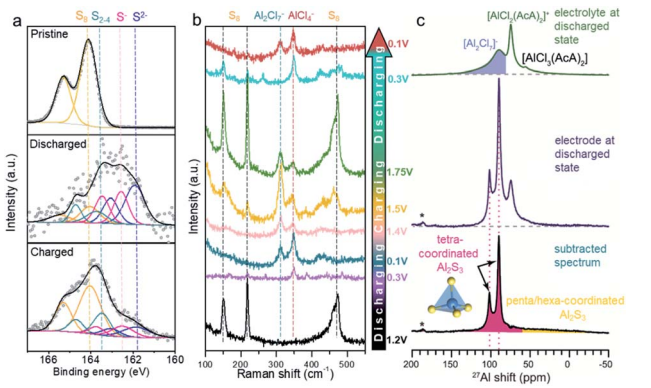

Fig. 4 (a) High-resolution XPS S 2p spectra of the cathodes before charge, charged at 1.75 V and discharged at 0.1 V. (b) *In situ* Raman spectra of the S cathode in electrochemical cycle processes. (c) ^{27}Al NMR spectra of the electrolyte and electrode at the discharged state extracted from the same Al–S@HPCK battery, recorded by magic-angle-spinning (MAS) at a frequency of 10 kHz. The bottom spectrum was obtained by the subtraction of the electrolyte spectrum (discharged state) from the electrode spectrum (discharged state). The peaks denoted with asterisks are identified as spinning sidebands (SSBs).

discharged state of 0.1 V, the spectra shift to lower binding energies owing to the reduction of elemental S. Especially, the fraction of S^{2-} is the largest among S-containing moieties at this state, suggesting the dominant transformation of S into Al_2S_3 during discharge.[22] The existence of elemental S and partially reduced S demonstrates an incomplete reduction reaction of the S cathode. Four peaks can be deconvoluted at 164.0 eV (area percentage 15.7%, the same below), 163.5 eV (19.3%), 162.5 eV (19.8%) and 161.8 eV (45.2%), corresponding to the elemental S_8, S_{2-4}, partially reduced S^- and fully reduced S^{2-}, respectively. In contrast, in the charged state, the S 2p spectrum largely returns to the pristine S state. Considering only S 2p3/2 peaks, four peaks can be deconvoluted at 164.0 eV (area percentage 54.2%, the same below), 163.5 eV (19%), 162.5 eV (12.2%) and 161.8 eV (14.6%), corresponding to the elemental S_8, S_{2-4}, partially reduced S^- and fully reduced S^{2-}, respectively. The results demonstrate that most aluminium sulfides formed in the discharge process can convert back to elemental S, including a large portion of S_8 and a relatively small portion of S_{2-4}.

In situ Raman spectroscopy was further employed to monitor the structural transformation and evaluate the reversibility of the S@HPCK cathode during the discharge and charge processes. As shown in Fig. 4b, at a nearly initial stage of 1.2 V, three major peaks are observed at 150, 219 and 470 cm^{-1}, which agree well with the characteristic Raman peaks of S_8 (Fig. S11†). No peaks attributed to $AlCl_4^-$ and $Al_2Cl_7^-$ ions are found in the detected region, suggesting that the electrolyte infiltration into the S-filled micropores of HPCK is slow. The phenomenon that the peaks of the electrolyte gradually appeared during the discharge process indicates that the electrolyte infiltration is largely driven by the electrochemical process, which may explain the activation of the battery (setting for 8 h before discharge) for ~10 cycles. When discharged to 0.3 V, the intensities of S_8 peaks become weakened, while a new peak at 347 cm^{-1} starts to appear, which can be attributed to the $AlCl_4^-$ ion from the electrolyte (Fig. S13†).[43,44] At the first end in the discharge state of 0.1 V, the signals of sulfur disappeared. Meanwhile, peaks of 314 and 347 cm^{-1} appeared, which belong to $Al_2Cl_7^-$ and $AlCl_4^-$ ions. Moreover, the $Al_2Cl_7^-/AlCl_4^-$ peak intensity ratio is sensitive to the $AlCl_3$/AcA molar ratio.[47] The $Al_2Cl_7^-/AlCl_4^-$ peak intensity ratio at the discharge state of 0.1 V obtained in the *in situ* Raman spectra is nearly identical to that in the $AlCl_3$/AcA (1.3/1) electrolyte (Fig. S13†), suggesting that the interfacial electrochemical reaction in this stage did not significantly alter the compositions of the $AlCl_3$/AcA (1.3/1) electrolyte trapped in the composite cathode. Then, with the further charging process, the S_8 peaks gradually appeared and enhanced at 1.75 V, clearly demonstrating the electrochemical reversibility of the S@HPCK cathode material. The variable $Al_2Cl_7^-/AlCl_4^-$ peak intensity ratio during the whole *in situ* Raman characterization is likely attributed to the concentration differences of $Al_2Cl_7^-$ and $AlCl_4^-$ ions in surface regions.

Due to the complicated electrochemical reaction procedures and minimized sizes of S, the discharge products may be highly amorphous, which can hardly be accurately identified by *in situ* XRD, *in situ* Raman and even TEM. Nuclear magnetic resonance (NMR) spectroscopy can characterize local chemical environments at the atomic level, regardless of the content of crystalline or amorphous structures. To further elucidate the mechanism of the Al–S electrochemistry, ^{27}Al NMR was conducted to identify the aforementioned materials. Since the electrolyte is hard to remove from the discharged electrode completely, the NMR spectrum of the electrolyte extracted from the discharged battery was first recorded to aid the analysis. As shown in Fig. 4c, the ssNMR spectrum of the $AlCl_3$/AcA (1.3/1) electrolyte at the discharged state possesses a sharp signal at 76 ppm attributed to $[AlCl_2(AcA)_2]^+$, and the broad signal ranging from 85 to 120 ppm stems from the coexisted $[AlCl_4]^-$ and $[Al_2Cl_7]^-$.[43,44] Additionally, a tiny peak is detected at 56 ppm, which is assigned to five-coordinated $[AlCl_3(AcA)_2]$.[43,48] As for the fully discharged electrode, the spectrum exhibits two new peaks at 102 and 90 ppm. Also, comparing the *in situ* Raman analysis in Fig. 4b and the intrinsic Raman spectra of $AlCl_3$/AcA (1.3/1) in Fig. S13,† it can be concluded that the composition of the adsorbed electrolyte in the fully discharged cathode at 0.1 V was not significantly changed. It means that the two sharp NMR peaks at 102 and 90 ppm, distinct from the NMR spectra of $AlCl_3$/AcA (1.3/1), should not be attributed to aluminium chloride species from the electrolyte. Therefore, the overall ^{27}Al NMR spectrum of the discharged electrode is the superposition of the Al-containing species in both the $AlCl_3$/AcA electrolyte and discharged sulfides.[49–51] The subtraction of the discharged state electrolyte spectrum from the discharged electrode spectrum gives the spectrum of the solely reduced products.

In aluminium sulfides, the tetra-coordinated (AlS_4) and hexa-coordinated (AlS_6) Al sites are located in downfield (~100 ppm) and upfield (~15 ppm) regions, which mainly exist in α (hexagonal structure)/β (hexagonal with a distorted wurtzite-type structure at high temperature/pressure) and γ (corundum-type structure) forms, respectively.[50,52] The split peaks at 90 and 102 ppm are characteristic of quadrupole interaction of ^{27}Al, and they can be assigned to the tetra-coordinated aluminium configuration (AlS_4) in Al_2S_3.[48–51] In addition, a very broad signal extends to around 0 ppm, reflecting a small amount of amorphous penta-/hexa-coordinated aluminium configuration (AlS_5/AlS_6) in Al_2S_3.[50] The quantity ratio of tetra-, penta- and hexa-coordinated Al_2S_3 is about 18 : 1 : 1 derived from the peak area intensity of NMR spectra. Furthermore, as shown in Fig. S22,† there is no signal observed at ~1650 ppm for the discharged electrode in the ^{27}Al NMR spectrum, indicating that metallic Al is not formed at the cathode upon cycling. Therefore, the ^{27}Al NMR investigation demonstrates the formation of Al_2S_3 at the cathode during discharge, which dominantly exists as tetra-coordination configuration in an α structure.

The formation of tetra-*versus* hexa-coordinated Al_2S_3 has been further studied by Density Functional Theory (DFT) calculations. Fig. 5a and b show the specific structures of tetra- and hexa-coordinated Al_2S_3, respectively. From thermodynamics, the formation energy (E_f) of tetra-coordinated Al_2S_3 is −25.14 eV $f.u.^{-1}$, lower than that of hexa-coordinated Al_2S_3 (−24.97 eV $f.u.^{-1}$). The bond energy (E_b) and bond length (L_b) of tetra-coordinated Al_2S_3 are −2.38 eV and 2.28 Å, respectively, in contrast to −1.55 eV and 2.43 Å for hexa-coordinated Al_2S_3

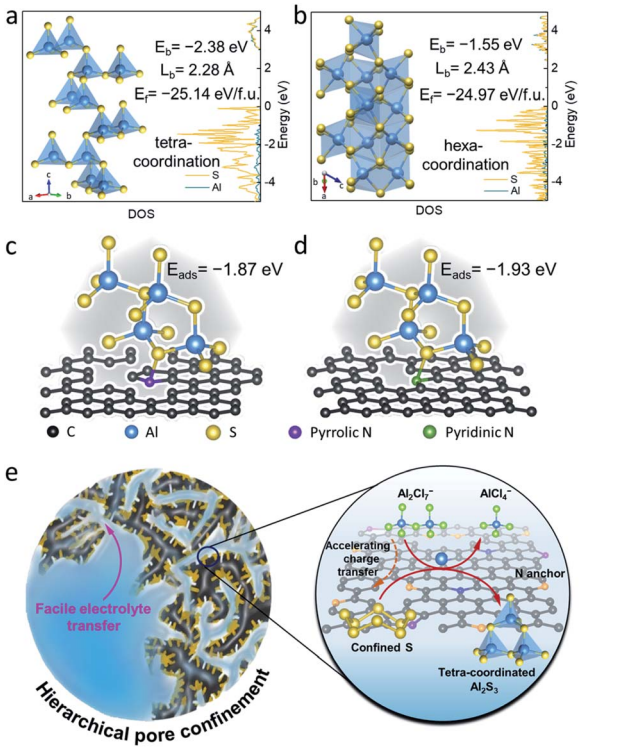

Fig. 5 (a, b) DOS results and specific structures of (a) tetra-coordinated Al_2S_3 and (b) hexa-coordinated Al_2S_3. E_f: formation energy (eV f.u.$^{-1}$), E_b: bond energy (eV), and L_b: bond length (Å). (c, d) Representative models and adsorbed energies of (c) pyrrolic N and (d) pyridinic N with tetra-coordinated Al_2S_3. (e) Schematic diagram showing the optimization effect and reaction mechanism of the S@HPCK cathode.

(Fig. 5a and b). The low E_f, low E_b and short L_b indicate that the tetra-coordinated Al_2S_3 is more easily formed than the hexa-coordinated Al_2S_3. Moreover, the densities of states (DOS) of the tetra-coordinated (Fig. 5a) and hexa-coordinated Al_2S_3 (Fig. 5b) reveal semiconducting features with bandgaps of ~3 eV, indicating the necessity of carbon composite materials to improve their conductivity.

To study the chemical effect of HPCK containing N dopants on the S cathode, we further calculated the DOS of S_8 and tetra-coordinated Al_2S_3 with graphitic carbon and N-doped graphitic carbon. As shown in Fig. S23,† a bandgap of 2.5 eV for S_8 is estimated from the DOS, which decreases but does not vanish when S_8 is associated with carbon. In contrast, the S@N-doped carbon system exhibits an increased DOS at the Fermi level, suggesting that the electrical conductivity of the system is significantly improved. Moreover, as shown in Fig. S24,† compared with the semiconductive Al_2S_3, the Al_2S_3@N-doped carbon system is metallic and increases the DOS at the Fermi level, indicating that the electrical conductivity has been significantly improved. Therefore, accelerated charge transfer processes owing to the N-doped carbon can be estimated during the electrochemical reactions. Meanwhile, the adsorption energies (E_{ads}) of pyrrolic N and pyridinic N with tetra-coordinated Al_2S_3 are −1.87 eV and −1.93 eV (Fig. 5c and d), respectively, suggesting the promising adsorbability of the N dopant centers with the discharged products of S. Therefore, the pyrrolic and pyridinic N atoms in the HPCK matrix are expected to anchor the S discharge products, leading to the enhanced cycle reversibility of the S@HPCK cathode.

Based on the above analysis, we outline the optimization effect and reaction mechanism of the S@HPCK cathode in Al–S batteries in Fig. 5e. The macropores in HPCK provide fast transport channels for the relatively viscous $AlCl_3$/AcA electrolyte, while the meso- and micro-pores confine the S nanoparticles within a small size range and thereby improve the electrochemical efficiency and suppress the structural collapse. The N-doped carbon matrix can also accelerate the charge transfer process owing to the high conductivity, which facilitates the dissociation of chloroaluminate ions and the reduction of S. The N dopant centers are good anchoring sites to suppress the separation and dissolution of the S discharge products, further enhancing the electrochemical efficiency and reversibility of the cathode. Importantly, owing to its low E_f, low E_b and short L_b compared with hexa-coordinated Al_2S_3, tetra-coordinated Al_2S_3 is more easily formed as the final discharge products of S in our study.

3. Conclusion

In summary, we have developed a N-doped carbon material with hierarchical micro-, meso-, and macro-pores and a high specific surface area of 2513 m^2 g^{-1}, which can significantly improve the electrochemical reversibility of S species by both physical confinement and chemical adsorption for high-performance Al–S batteries. The hierarchical pore structure can promote electrolyte transport and electrochemical reaction efficiency, while the N-doped carbon can facilitate charge transfer to accelerate reactions and anchor aluminium sulfides to suppress cathode deterioration. Coupled with a low-cost $AlCl_3$/AcA (1.3/1) electrolyte, the S composite cathode can deliver excellent electrochemical performance, including an initial capacity of 1583 mA h g^{-1} and a retention of 1027 mA h g^{-1} after 50 cycles. In particular, the as-derived Al–S batteries show excellent cycle stability, with a capacity of 483/405 mA h g^{-1} after 500/700 cycles at 1 A g^{-1}. The Al–S electrochemical mechanism was investigated by XPS, *in situ* Raman and ssNMR, demonstrating the reversible transformation of the S active material in the composite cathode and α-type Al_2S_3 with a tetra-coordinated configuration as the dominant final discharge product. The enhanced performance of the Al–S battery by the N-doped hierarchical porous carbon as the S host was further explained based on DFT calculations with the N-doped carbon structure and derived product configuration. This study provides a new strategy to improve the long-term cycle reversibility of rechargeable Al–S batteries, and also sheds light on the understanding of the reaction mechanism of Al–S electrochemistry.

4. Experimental

4.1 Materials preparation

The KOH-etched N-doped hierarchical porous carbon (HPCK) was synthesized in two steps. Firstly, diaminodiphenylmethane

(1.98 g), polyformaldehyde (0.75 g), zinc nitrate hexahydrate (8.91 g) and *N*-methyl pyrrolidone (NMP, 20 mL) were added into a high-pressure reaction bottle under argon, and the mixture was stirred at 100 °C for 4 h to produce a polymer solution. Then, the polymer solution containing zinc nitrate hexahydrate was insulated in an argon-protected tube furnace at 120 °C for 6 h, heated to 900 °C from 120 °C in 2 h, and kept at 900 °C for 2 h at a pressure of 0.1 atm, yielding a foam-like carbon material (HPC). Secondly, KOH and HPC in a weight ratio of 3 : 1 were ground uniformly for 30 min in an argon glovebox. The mixture was then heated to 800 °C with a ramp rate of 2 °C min^{-1}, and then held at 800 °C for 2 h in argon. After cooling, the mixture was washed with diluted HCl and H_2O to yield the final HPCK.

The S@HPCK composite was prepared according to our previous report.[24] Typically, HPCK and S were ground in a mortar at a designed weight ratio for 30 min. The mixture was then transferred into a hydrothermal reactor under argon and heated at 155 °C for 12 h to yield the final S@HPCK composite.

4.2 Preparation of the electrolyte

$AlCl_3$/acetamide (molar ratio 1.3/1) was prepared according to our previous work.[24] All processes were carried out inside an argon-protected Mikrouna glovebox (H_2O and O_2 are below 1 ppm) at room temperature. Anhydrous aluminium chloride ($AlCl_3$, 99%, Acklin) was slowly added into acetamide (AcA, 99%, Aladdin) under stirring. The mixture was further stirred overnight to produce a liquid deep eutectic solvent as the electrolyte.

4.3 Battery assembly

The S@HPCK cathode was prepared by drying a slurry containing 80 wt% S@HPCK with 10 wt% PTFE binder and 10 wt% acetylene black. The areal loading of S per unit area was around 1.0 mg cm^{-2}. Al–S batteries were assembled in a Swagelok configuration, with the S@HPCK cathode, Al foil (99.9%, 0.05 mm, Beijing Trillion Metals Co., Ltd) as the anode, ~100 μL $AlCl_3$/AcA (1.3/1) as the electrolyte, Whatman glass fiber as the separator, and a molybdenum network as the current collector.

4.4 Electrochemical analysis and characterization

The electrochemical performance of Al–S batteries were tested using Land instruments (Wuhan LAND Electronics Co., Ltd). The capacity was calculated based on the mass of S. Cyclic voltammetry (CV) was performed using a Solartron electrochemical workstation.

XRD patterns were obtained on a Bruker D8 Advance Diffractometer using CuKα radiation. Scanning electron microscopy (SEM) was conducted using a Hitachi S-4800 instrument. Transmission electron microscopy (TEM) was carried using a JEM-2100F instrument. The Raman spectra of electrolytes (sealed in quartz boats to prevent the influences of O_2 and moisture) were acquired using a Raman spectrometer (WITec GmbH) with a 532 laser. *In situ* Raman investigation was performed using the same system coupled with a home-made *in situ* electrochemical cell. TGA was conducted with a heating rate of 10 °C min^{-1} in a N_2 atmosphere from 25 to 600 °C using a Labsys evo (France) analyzer.

X-ray photoelectron spectra (XPS) were acquired with a Thermo Scientific ESCALAB 250Xi spectrometer, using monochromatized Al Kα X-rays (1486.7 eV). The samples were prepared in an argon glovebox and transferred into the XPS chamber with argon protection. Before measurement, samples were etched with Ar^+ to eliminate the influences of O_2 and H_2O. Data were fitted with a Lorentzian–Gaussian (30%/70%) function and a Shirley background. S 2p spectra were fitted with spin–orbit split 2p3/2 and 2p1/2 doublets under a constrain of 1.18 eV splitting and a characteristic 2 : 1 area ratio.

N_2 adsorption/desorption analysis was conducted by degasification at 200 °C for 12 h using an automatic physical adsorption analyzer (ASAP 2020HD88). The specific surface areas were calculated based on the multi-point Brunauer–Emmett–Teller (BET) method. Pore size distribution (PSD) curves were recorded using the density functional theory (DFT) method. Specific pore volume was calculated using the Dubinin–Radushkevich equation.

The *in situ* Raman spectra were recorded on a confocal Raman microscope (Wetic, German) with an excitation wavelength of 532 nm during the electrochemical cycling of an *in situ* battery (Beijing Science Star Technology Co. Ltd).

^{27}Al Nuclear Magnetic Resonance (NMR) spectra were acquired on a Bruker 400 MHz spectrometer (AVANCE HD III, Germany), which is equipped with a Bruker 4.0 mm double resonance MAS probe. The Larmor frequency for the ^{27}Al isotope is 104.28 MHz. All studied materials were packed into 4.0 mm zirconia rotors inside an argon-filled glovebox. For the discharged electrode, the spinning rate was set as 10 kHz controlled with a Bruker pneumatic MAS unit. The other samples were measured under static conditions. A single pulse of 2.9 μs was set for 90° excitation. A total of 64 scans were accumulated for all samples to get a reasonable signal. The ^{27}Al shifts were referenced to an external solution of 1.0 mol L^{-1} $Al(NO_3)_3$ in D_2O with a shift value of 0 ppm.

4.5 The first-principles calculation

The first-principles calculation was performed by using the Vienna Ab Initio Package (VASP) to realize the density functional theory (DFT) calculation, using the projector augmented wave (PAW) to describe the interaction between ions and electrons. The plane-wave basis is cut off by 520 eV. For the optimization of the crystal structure, the generalized gradient approximation (GGA) was adopted in the parameterization of Perdew, Burke, and Ernzerhof (PBE) to describe the exchange–correlation function. The lattice vector and the atomic position are sufficiently optimized until the resultant force per atom is less than 0.01 eV $Å^{-1}$ using a 3 × 3 × 2 *Γ*-centered *k*-mesh.

Conflicts of interest

There are no conflicts to declare.

Acknowledgements

This work was supported by the National Natural Science Foundation of China (Grants 22075007, 21975006, 21875007, 51802009, and 21974007), Beijing Natural Science Foundation (JQ19003, KZ201910005002, KZ202010005007 and L182009), the National Key R&D Program of China (Grant No. 2018YFB0104302) and the Project of Youth Talent Plan of Beijing Municipal Education Commission (CIT&TCD201804013).

References

1 J. Muldoon, C. B. Bucur and T. Gregory, *Chem. Rev.*, 2014, **114**, 11683–11720.
2 D. Larcher and J. M. Tarascon, *Nat. Chem.*, 2015, **7**, 19–29.
3 M. C. Lin, M. Gong, B. Lu, Y. Wu, D. Y. Wang, M. Guan, M. Angell, C. Chen, J. Yang, B. J. Hwang and H. Dai, *Nature*, 2015, **520**, 325–328.
4 G. A. Elia, K. Marquardt, K. Hoeppner, S. Fantini, R. Lin, E. Knipping, W. Peters, J. F. Drillet, S. Passerini and R. Hahn, *Adv. Mater.*, 2016, **28**, 7564–7579.
5 Y. Zhang, S. Liu, Y. Ji, J. Ma and H. Yu, *Adv. Mater.*, 2018, **30**, e1706310.
6 H. Yang, H. Li, J. Li, Z. Sun, K. He, H. M. Cheng and F. Li, *Angew. Chem., Int. Ed.*, 2019, **58**, 11978–11996.
7 D. Y. Wang, C. Y. Wei, M. C. Lin, C. J. Pan, H. L. Chou, H. A. Chen, M. Gong, Y. Wu, C. Yuan, M. Angell, Y. J. Hsieh, Y. H. Chen, C. Y. Wen, C. W. Chen, B. J. Hwang, C. C. Chen and H. Dai, *Nat. Commun.*, 2017, **8**, 14283.
8 M. Angell, C. J. Pan, Y. Rong, C. Yuan, M. C. Lin, B. J. Hwang and H. Dai, *Proc. Natl. Acad. Sci. U. S. A.*, 2017, **114**, 834–839.
9 H. Chen, F. Guo, Y. Liu, T. Huang, B. Zheng, N. Ananth, Z. Xu, W. Gao and C. Gao, *Adv. Mater.*, 2017, **29**, 1605958.
10 Z. Liu, J. Wang, H. Ding, S. Chen, X. Yu and B. Lu, *ACS Nano*, 2018, **12**, 8456–8466.
11 J. Wang, X. Zhang, W. Chu, S. Liu and H. Yu, *Chem. Commun.*, 2019, **55**, 2138–2141.
12 S. Jiao, H. Lei, J. Tu, J. Zhu, J. Wang and X. Mao, *Carbon*, 2016, **109**, 276–281.
13 H. Chen, H. Xu, S. Wang, T. Huang, J. Xi, S. Cai, F. Guo, Z. Xu, W. Gao and C. Gao, *Sci. Adv.*, 2017, **3**, eaao7233.
14 N. Jayaprakash, S. K. Das and L. A. Archer, *Chem. Commun.*, 2011, **47**, 12610–12612.
15 T. Koketsu, J. Ma, B. J. Morgan, M. Body, C. Legein, W. Dachraoui, M. Giannini, A. Demortiere, M. Salanne, F. Dardoize, H. Groult, O. J. Borkiewicz, K. W. Chapman, P. Strasser and D. Dambournet, *Nat. Mater.*, 2017, **16**, 1142–1148.
16 S. He, J. Wang, X. Zhang, J. Chen, Z. Wang, T. Yang, Z. Liu, Y. Liang, B. Wang, S. Liu, L. Zhang, J. Huang, J. Huang, L. A. O'Dell and H. Yu, *Adv. Funct. Mater.*, 2019, **29**, 1905228.
17 C. Wu, S. Gu, Q. Zhang, Y. Bai, M. Li, Y. Yuan, H. Wang, X. Liu, Y. Yuan, N. Zhu, F. Wu, H. Li, L. Gu and J. Lu, *Nat. Commun.*, 2019, **10**, 73.
18 K. Liang, L. Ju, S. Koul, A. Kushima and Y. Yang, *Adv. Energy Mater.*, 2019, **9**, 1802543.
19 L. Geng, J. P. Scheifers, J. Zhang, K. N. Bozhilov, B. P. T. Fokwa and J. Guo, *Chem. Mater.*, 2018, **30**, 8420–8425.
20 H. Li, H. Yang, Z. Sun, Y. Shi, H.-M. Cheng and F. Li, *Nano Energy*, 2019, **56**, 100–108.
21 S. Wang, Z. Yu, J. Tu, J. Wang, D. Tian, Y. Liu and S. Jiao, *Adv. Energy Mater.*, 2016, **6**, 1600137.
22 T. Gao, X. Li, X. Wang, J. Hu, F. Han, X. Fan, L. Suo, A. J. Pearse, S. B. Lee, G. W. Rubloff, K. J. Gaskell, M. Noked and C. Wang, *Angew. Chem., Int. Ed.*, 2016, **55**, 9898–9901.
23 X. Yu, M. J. Boyer, G. S. Hwang and A. Manthiram, *Chem*, 2018, **4**, 586–598.
24 W. Chu, X. Zhang, J. Wang, S. Zhao, S. Liu and H. Yu, *Energy Storage Mater.*, 2019, **22**, 418–423.
25 G. Cohn, L. Ma and L. A. Archer, *J. Power Sources*, 2015, **283**, 416–422.
26 H. Yang, L. Yin, J. Liang, Z. Sun, Y. Wang, H. Li, K. He, L. Ma, Z. Peng, S. Qiu, C. Sun, H. M. Cheng and F. Li, *Angew. Chem., Int. Ed.*, 2018, **57**, 1898–1902.
27 X. Yu and A. Manthiram, *Adv. Energy Mater.*, 2017, **7**, 1700561.
28 W. Li, Z. Liang, Z. Lu, H. Yao, Z. W. Seh, K. Yan, G. Zheng and Y. Cui, *Adv. Energy Mater.*, 2015, **5**, 1500211.
29 Z. L. Xu, S. Lin, N. Onofrio, L. Zhou, F. Shi, W. Lu, K. Kang, Q. Zhang and S. P. Lau, *Nat. Commun.*, 2018, **9**, 4164.
30 S. Xin, L. Gu, N. H. Zhao, Y. X. Yin, L. J. Zhou, Y. G. Guo and L. J. Wan, *J. Am. Chem. Soc.*, 2012, **134**, 18510–18513.
31 S. Liu, X. Zhang, S. He, Y. Tang, J. Wang, B. Wang, S. Zhao, H. Su, Y. Ren, L. Zhang, J. Huang, H. Yu and K. Amine, *Nano Energy*, 2019, **66**, 104159.
32 X. Huang, Y. Liu, C. Liu, J. Zhang, O. Noonan and C. Yu, *Chem. Sci.*, 2018, **9**, 5178–5182.
33 X. Ji, K. T. Lee and L. F. Nazar, *Nat. Mater.*, 2009, **8**, 500–506.
34 W. Wang, Z. Cao, G. A. Elia, Y. Wu, W. Wahyudi, E. Abou-Hamad, A.-H. Emwas, L. Cavallo, L.-J. Li and J. Ming, *ACS Energy Lett.*, 2018, **3**, 2899–2907.
35 G. Zhu, M. Angell, C.-J. Pan, M.-C. Lin, H. Chen, C.-J. Huang, J. Lin, A. J. Achazi, P. Kaghazchi, B.-J. Hwang and H. Dai, *RSC Adv.*, 2019, **9**, 11322–11330.
36 N. Ding, X. Li, S. W. Chien, Z. Liu and Y. Zong, *Chem. Commun.*, 2017, **53**, 10152–10155.
37 J. Zheng, G. Ji, X. Fan, J. Chen, Q. Li, H. Wang, Y. Yang, K. C. DeMella, S. R. Raghavan and C. Wang, *Adv. Energy Mater.*, 2019, **9**, 1803774.
38 P. Hu, W. Jiang, L. Zhong and S. Zhou, *Chin. J. Chem. Eng.*, 2019, **27**, 144–149.
39 J. M. Garcia, G. O. Jones, K. Virwani, B. D. McCloskey, D. J. Boday, G. M. ter Huurne, H. W. Horn, D. J. Coady, A. M. Bintaleb, A. M. Alabdulrahman, F. Alsewailem, H. A. Almegren and J. L. Hedrick, *Science*, 2014, **344**, 732–735.
40 Y. Yamada, J. Kim, S. Matsuo and S. Sato, *Carbon*, 2014, **70**, 59–74.
41 Y. Qiu, W. Li, W. Zhao, G. Li, Y. Hou, M. Liu, L. Zhou, F. Ye, H. Li, Z. Wei, S. Yang, W. Duan, Y. Ye, J. Guo and Y. Zhang, *Nano Lett.*, 2014, **14**, 4821–4827.

42 J.-J. Chen, R.-M. Yuan, J.-M. Feng, Q. Zhang, J.-X. Huang, G. Fu, M.-S. Zheng, B. Ren and Q.-F. Dong, *Chem. Mater.*, 2015, **27**, 2048–2055.
43 P. Hu, R. Zhang, X. Meng, H. Liu, C. Xu and Z. Liu, *Inorg. Chem.*, 2016, **55**, 2374–2380.
44 F. Coleman, G. Srinivasan and M. Swadzba-Kwasny, *Angew. Chem., Int. Ed.*, 2013, **52**, 12582–12586.
45 Y. Guo, H. Jin, Z. Qi, Z. Hu, H. Ji and L.-J. Wan, *Adv. Funct. Mater.*, 2019, **29**, 1807676.
46 Y. Guo, Z. Hu, J. Wang, Z. Peng, J. Zhu, H. Ji and L. J. Wan, *Angew. Chem., Int. Ed.*, 2020, **59**, 22963–22967.
47 C. Liu, W. Chen, Z. Wu, B. Gao, X. Hu, Z. Shi and Z. Wang, *J. Mol. Liq.*, 2017, **247**, 57–63.
48 M. Haouas, F. Taulelle and C. Martineau, *Prog. Nucl. Magn. Reson. Spectrosc.*, 2016, **94–95**, 11–36.
49 A. Lafond, X. Rocquefelte, M. Paris, C. Guillot-Deudon and V. Jouenne, *Chem. Mater.*, 2011, **23**, 5168–5176.
50 W. S. Jung and S. K. Ahn, *Mater. Lett.*, 2000, **43**, 53–56.
51 S. M. Martin and J. A. Sills, *J. Non-Cryst. Solids*, 1991, **135**, 171–181.
52 E. E. Hellstorm and R. A. Huggins, *Mater. Res. Bull.*, 1979, **14**, 881–889.

